Review of Scientific Instruments ARTICLE scitation.org/journal/rsi

Pulsed electron gun for electron diffraction at surfaces with femtosecond temporal resolution and high coherence length

Cite as: Rev. Sci. Instrum. 90, 045119 (2019); doi: 10.1063/1.5086124
Submitted: 18 December 2018 • Accepted: 20 March 2019 •
Published Online: 19 April 2019

B. Hafke,[1] T. Witte,[1,a)] C. Brand,[1] Th. Duden,[2] and M. Horn-von Hoegen[1]

AFFILIATIONS

[1] Department of Physics and Center for Nanointegration CENIDE, University of Duisburg-Essen, Lotharstraße 1, 47057 Duisburg, Germany
[2] Th. Duden Konstruktionsbüro, Borgsen-Allee 35, 33649 Bielefeld, Germany

[a)] **Electronic mail:** tobias.witte@uni-due.de

ABSTRACT

We present a newly designed 30 kV pulsed electron gun for ultrafast electron diffraction suited for pump-probe setups driven by femtosecond laser pulses. The electron gun can be operated both in transmission and reflection geometry. A robust design with a back illuminated Au photocathode, extraction fields of 7.5 kV/mm, and a magnetic focus lens ensures reliable daily use. Magnetic deflectors allow for beam alignment and characterization. Focusing of the UV pulse on the photocathode results in a small source size of photoemitted electrons and thus a high transverse coherence length of more than 50 nm in diffraction. A low difference of $\Delta E = 0.1$ eV between the work function of the 10 nm Au photocathode and photon energy of the frequency tripled UV laser pulses results in an instrumental temporal resolution of 330 fs full width at half maximum. This resolution is discussed with respect to the number of electrons per pulse.

I. INTRODUCTION

The dynamical response of condensed matter systems subsequent to an ultrashort external stimulus is typically investigated by techniques following a pump-probe scheme. Usually a femtosecond laser pulse is employed as a pump pulse. The transient response of the system is investigated by an ultrashort probe pulse at variable time delays Δt to the pump pulse. Depending on the physical property that is investigated, different probes may be used. Using another photon pulse leading to photoemission of the initially excited electrons allows studies on the properties of the electron system. The analysis of energy and momentum of the photoelectrons yields insight into the population dynamics,[1] as well as transient changes in the electronic structure.[2] Using electrons or X-rays as probe that are diffracted at the sample allows analyses of the structural dynamics of the atoms' core positions with sub-angstrom spatial and femtosecond temporal resolution.[3–7]

Pioneering studies employing ultrafast electron diffraction in transmission provided insight into the structural dynamics of chemical reactions,[8–10] melting processes,[11–13] phase transformations,[14–16] or phonon-phonon interactions.[17,18] Surface sensitivity can be achieved either through low energy electrons under normal incidence[19] or through high energy electrons under grazing incidence in a reflection geometry.[20–25]

Surface diffraction has been utilized in studies of nanoscale heat transport from ultrathin films or nanostructures,[26–28] dynamics[20–22] and mode conversion in adsorbate layers,[29] and driven structural transitions.[19,30,31]

Here, we present a new design for a pulsed electron gun for energies up to 30 keV, providing ultrashort electron pulses for both reflection and transmission diffraction without the usage of a pulse compression. To benchmark the temporal properties of this new gun, the ultrafast $(8 \times 2) \leftrightarrow (4 \times 1)$ phase transition of In/Si(111) after intense infrared optical excitation was used. With excitation fluences above 3 mJ/cm^2, the phase transition can be as fast as $\tau_{\mathrm{dec}} = 350$ fs.[32] The overall temporal resolution of our entire experimental setup was found to be of $\delta_{\mathrm{FWHM}} = 330$ fs full width at half maximum (FWHM; 140 fs RMS).

This high temporal resolution is attributed to the work function of the employed photocathode being almost equal to the energy of the UV photon dislodging electrons, to a high acceleration field and short traveling distances. A coherence length of $\xi_\perp \approx 50$ nm is achieved by the combination of a small photoelectron source together with low magnification onto the detector.

II. EXPERIMENTAL SETUP

Figure 1 shows an overall setup of the experiment (a) and a detailed view of the gun (b). Short laser pulses are generated from a commercial oscillator (Micra, Coherent) at a repetition rate of 80 MHz and an output power of 350 mW. These pulses are amplified in a regenerative amplifier (Legend, Coherent) to 80 fs short laser pulses at 5 kHz repetition rate and 1 mJ energy. The pulses are split (80/20) into two parts. The more intense part serves as pump pulse to excite the sample. The less intense part is split into two equal parts (50/50): The first part is used for pulse-characterization through frequency optical gating.[33] The second part is guided through an opto-mechanical delay line which enables to temporally delay this pulse with respect to the pump pulse. It is then narrowed by a factor of 4 using a telescope and directed through two barium borate (BaB_2O_4, BBO) crystals creating third harmonic light (wavelength 266 nm). In front of the BBO crystals, a $\lambda/2$-waveplate is mounted which enables variation of the intensity of the UV pulse through slight degradation of the phase matching in the BBOs. Dielectric mirrors are used to route the UV pulse to the electron gun while dumping remnants of the fundamental and frequency doubled laser pulse. Using a refractive lens with a focal length of 200 mm, the third harmonic is focused and fed onto the photocathode inside the ultra-high vacuum (UHV) chamber [see Fig. 1(b)].

The photocathode consists of a 10 nm thin gold film that was deposited onto a tungsten coated (2 nm thin film) sapphire substrate (diameter 20 mm). The tungsten film serves as an adhesive to increase the photocathode lifetime. The photocathode is prepared in another vacuum chamber and subsequently transferred into the gun-assembly. Because of the initial tungsten coating, the photocathode can withstand the bake-out procedure at 140 °C for several days. The overall lifetime of such a photocathode exceeded a year of usage with multiple bake-out procedures.

Via an one-photon-photo-emission process, the UV pulse generates an electron pulse. The number of electrons in the pulse can be adjusted by decreasing the intensity of the UV pulse through rotation of the $\lambda/2$-waveplate in front of the BBO crystals as mentioned before. It has to be noted that the pulse directed onto the photocathode still contains portions of the fundamental (800 nm) and second harmonic (400 nm). These remnants, however, are of such low intensity that photo-emission via a two- or three-photon process is negligible. As has been reported in an earlier study, the initial energy broadening of the photo-emitted electrons is around $\Delta E = 0.1$ eV.[23] This narrow initial energy width is assigned to the reduced work function of thin gold films as compared to gold bulk, which is 0.1 eV smaller than the energy of the UV photons ($3h\nu = 4.65$ eV) for the 10 nm thin gold film.

The pulsed electron gun is mounted on a custom-made DN 150 CF flange with an integrated window and a 15-pin feedthrough serving as electric connection for the magnetic lens and the deflector coils [see Fig. 1(b)]. The gun consists of a retainer plate, a cathode holder, and the magnetic lens assembly. These parts are electrically isolated by ceramic spheres of 20 mm diameter. The retainer plate and the magnetic lens assembly are at ground potential, whereas the cathode holder is connected to the high voltage power supply

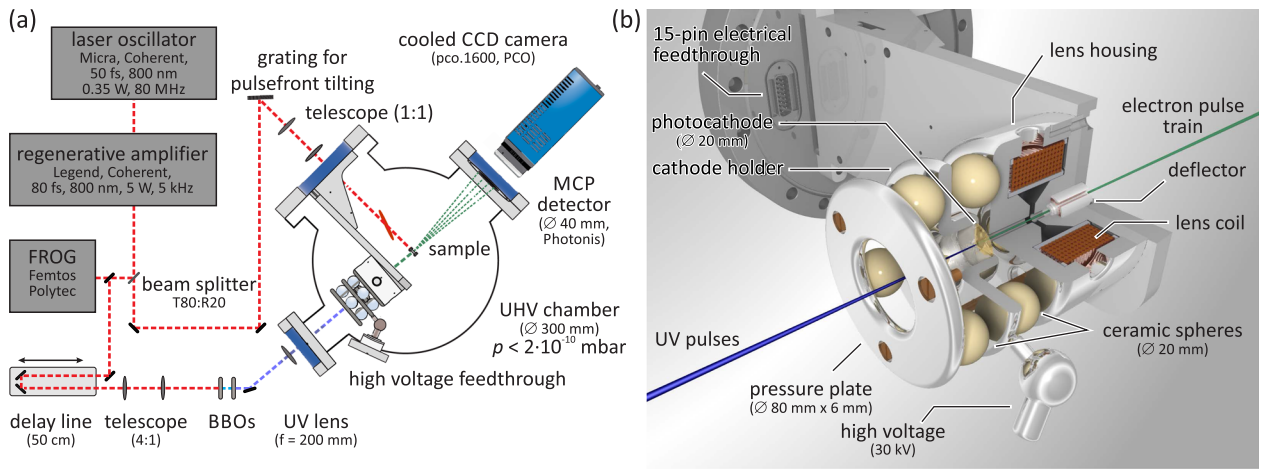

FIG. 1. (a) Schematic setup of the time-resolved electron diffraction experiment. All but the ultra-high vacuum (UHV) chamber ($p < 2 \times 10^{-10}$ mbar) and electron gun are unscaled. The laser amplifiers output is constantly monitored by frequency resolved optical gating (Femtos, Polytec). Both pump and probe pulses are separately stabilized against pointing instability (MRC systems). (b) Detailed 3D view of the pulsed electron source. The whole gun is assembled on a DN 150 CF custom made flange with integrated 15-pin feedthrough for the electrical connection and viewport for the pump pulse (not visible in the figure). The lens housing is made from high μ-material (Permenorm, Vacuumschmelze). The coils are made from Kapton®-insulated copper wires with diameters of 1 mm and 0.25 mm for the focus lens and deflector coils, respectively. The magnetic lens is not actively cooled. The insulation spheres (Friederichsfeld) are 20 mm in diameter and made from dense ceramic Al_2O_3. All other parts are made from aluminum. The high voltage is fed separately into the chamber.

through a high voltage feedthrough. The default operating voltage is 30 kV. All elements are carefully polished with no sharp edges to avoid arcing. The distance of 4 mm between the photocathode and the magnetic lens assembly, which serves as anode, yields an electric field of E_{acc} = 7.5 kV/mm. This leads to rare arcing at the photocathode and allows for measurement time of several hours. Additionally, the large area of the photocathode and the large anode hole (diameter of 4 mm) result in smooth electrical field lines without large gradients in front of the anode. This reduces the divergence of the electron beam resulting in a reduced requirement of the focusing lens. However, in order to obtain a high spatial resolution (coherence length/transfer width), the source of the electron pulse has to be small. This is achieved by focusing the UV-light pulse onto the photocathode.

The solenoid of the magnetic lens has 286 windings of Kapton-insulated copper wire of 1 mm diameter. The yoke of the magnetic lens consists of two pole pieces made from a magnetically soft, high-μ material (Permenorm 5000 H2). The gap in the yoke amounts to 4 mm. To assure high magnetic coupling between the two yokes, their contact areas have been lapped plane-parallel. At typical conditions at 30 kV, the lens operates at a current of I_{lens} = 1.5 A.

At the exit of the magnetic lens, a XY deflector has been integrated which is composed of two split pair coils each made of 30 windings of Kapton-insulated copper wires of 0.25 mm diameter. With this, the electron beam can be manipulated as shown in Sec. III.

The electrons then scatter under a grazing angle of incidence θ = 1°–6° at the surface of the sample, which is placed 50 mm behind the gun exit aperture. The diffracted electrons are amplified through a microchannel plate (MCP, Burle, diameter: 40 mm) and recorded by a cooled CCD camera (pco.1600, PCO). With respect to the direction of the initial electron path, the center of the MCP detector is rotated by 11° [see Fig. 1(a)]. The distance between the MCP and the sample is 190 mm. With these parameters, diffraction from the zeroth and first order Laue circle of a Si(111) sample is observable and the corresponding diffraction spots can be recorded simultaneously (see Sec. IV).

III. FOCUSING, DEFLECTION, AND TRANSFER WIDTH

Figure 2 depicts the focusing properties of the magnetic lens. The incident electron beam at an energy of E_0 = 30 keV is directly imaged on the MCP by deflecting the beam through the XY deflector. Figures 2(a) and 2(b) compares the effect of the magnetic lens for an unfocused UV beam. In Fig. 2(a), a triangular caustic of the broad electron beam with an almost symmetric intensity is observed. Applying a lens current of I_{lens} = 1.42 A to the magnetic lens reduces the beam size, but still a non-circular shaped electron spot is observed [see Fig. 2(b)]. Spot profiles are shown in the vertical (red) and horizontal (blue) directions in Figs. 2(b) and 2(d). As the gun is rotationally symmetric, the reason for the threefold astigmatism is ascribed to mechanical deformation in the gun during assembly.

Figures 2(c) and 2(d) compare the same settings but using a focused UV beam for photoexcitation with a focal diameter of 25 μm, resulting in a smaller electron source spot. In Fig. 2(c), the triangular shape is still visible but less pronounced. In contrast to

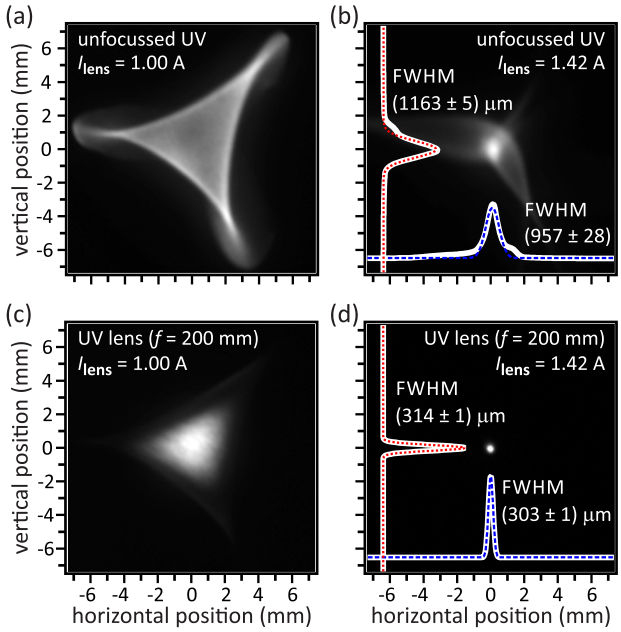

FIG. 2. Two-dimensional intensity distributions of the direct pulsed electron beam. The 30 keV electron beam has been deflected onto the MCP for direct imaging. (a) and (b) show the electron beam image with unfocussed UV pulses at lens currents of I_{lens} = 1.0 A and 1.42 A, respectively. For (c) and (d), the UV pulses were focused onto the photocathode. In (b) and (d), the white lines depict intensity line profiles along the respective directions. The red and blue curves are Gaussian fits to the line profiles. The threefold astigmatism in (a)–(c) is ascribed to mechanical tension in the lens housing during assembly.

Fig. 2(a), the beam now exhibits a maximum in the center of the triangle. Applying a current of 1.42 A to the magnetic lens results in a well focused and circular-shaped electron beam as evident from the spot profiles [see Fig. 2(d)].

Figure 3(a) shows the maximum intensity of the electron beam for focus lens currents 1 A < I_{lens} < 2 A. The maximum intensity was found at a lens current of 1.42 A. Fitting the electron beam signal [see the inset of Fig. 3(a)] with a two-dimensional Gaussian function yields the FWHM of the beam profile, as shown in Fig. 3(b). Starting with a FWHM of approximately 1 mm for both directions at I_{lens} = 1 A, the width reduces to a minimum of about 300 μm at 1.42 A and increases again for larger lens currents. The minimum beam sizes in the two directions are found at I_{lens} = 1.42 A and 1.5 A for the horizontal and vertical directions, respectively. This twofold astigmatism is very likely caused by the deflection element. In future versions, we will employ an integrated stigmator deflector to address this and the above mentioned threefold astigmatism. The correlation between the two directions shows a minimum at I_{lens} = 1.56 A. At this current, the beam image is circular-shaped with a FWHM of 450 μm. During operation, we set the lens current to the value resulting in the maximum intensity and accepting the slight deviation from a circular shaped beam profile.

The lens current I_{lens} for the smallest beam size depends on the electron energy E_0, as shown in Fig. 3(c). The functional dependence seems to be linear in the given energy window. However, evaluating the refractive power of a thin magnetic lens on an electron beam

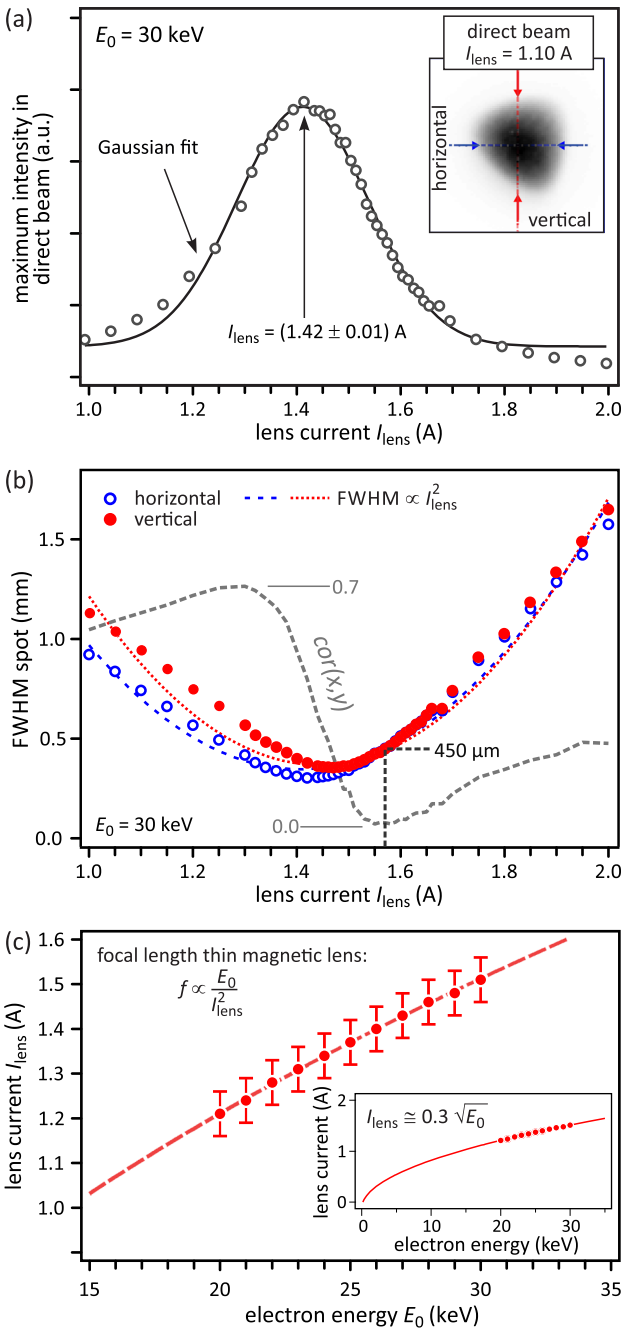

FIG. 3. Magnetic lens properties. The direct beam image [inset in (a)] has been fitted by a two-dimensional Gaussian profile. (a) The maximum intensity of the 2D-fit is displayed, which exhibits a maximum at a lens current of I_{lens} = 1.42 A. (b) shows the FWHM of the horizontal and vertical beam profiles. The minimum widths are found between I_{lens} = 1.42 A and 1.5 A. However, a fully rotationally symmetric profile is only found at I_{lens} = 1.57 A (cor(x, y) = 0) with the function cor(x, y) as a measure of the rotational symmetry of the beam profile. (c) shows the dependence of the lens current on different electron energies. The observed dependence follows the $\sqrt{E_0}$-behavior expected for a thin magnetic lens (see the inset), which exhibits an almost linear behavior between 20 and 30 keV.

results in a $\sqrt{E_0}$-dependence, which describes the observed data well (see the inset of Fig. 3). Although the whole setup has been designed for an electron energy of E_0 = 30 keV, studies at smaller or higher energies are possible.

It is noted that the smallest beam size with best symmetry is only achieved if the focus of the UV beam coincides with the gun optical axis and which therefore has to be carefully adjusted. The adjustment is obtained through defocusing the electron beam which results in the image shown in Fig. 2(c). Then, the position of the UV beam is laterally shifted until the maximum intensity is found in the center of the triangle. With changing focus lens current, the electron beam must not move. This way the optical axes of the UV pulse and the electron gun can be aligned. During the experiment, a feedback loop with piezoactuators (MRC systems) assures pointing stability of the laser beam and thus alignment with the electron gun.

Integrated into the lens housing is a XY deflector. As shown in Fig. 4, the electron beam can be deflected by approximately ±7.5°/A deflection current $I_{deflect}$. For simplicity, Fig. 4 only shows one direction. By reversing the current direction, deflection in the opposite direction is obtained. The inset shows that the deflection directions are tilted by 14° with respect to the MCP axes. This can be compensated by controlling both deflection currents electronically.

The deflector is mainly used to characterize the electron beam itself by deflection onto the MCP as described above. With the electron source and the MCP detector being spatially fixed and having to coincide with the pump laser at the sample, the deflector can further be used for aligning the electron beam axis with the aforementioned. It may also be used to address missing degrees of freedom of the sample (e.g., azimuthal angle), but requires repositioning of the sample in the chamber.

The coherence length or transfer width ξ is a measure for electron diffraction setups reflecting the resolution power in real

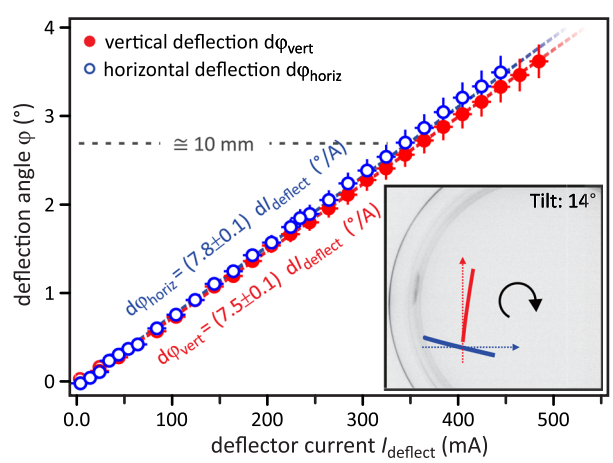

FIG. 4. The beam deflector exhibits a linear relationship between deflection angle φ and deflector current $I_{deflect}$ both in horizontal (blue circles) and vertical (red dots) directions. A deflection by 2.8° results in a 10 mm displacement on the screen. Polarity reversal of the deflector current causes reversed deflection. The inset shows that the deflection direction is tilted with respect to the global coordinate system that is given by the sample position (arrows in the inset). This can be compensated electronically.

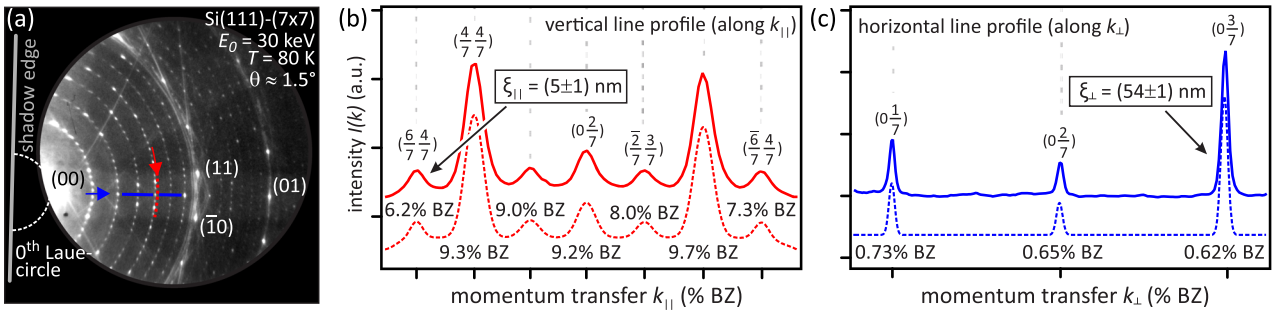

FIG. 5. (a) Diffraction pattern of a (7 × 7) reconstructed Si(111) surface. The electron energy is 30 ke,V and the incident angle is about 1.5°. Zeroth, first, and second Laue circles are visible. Some of the main diffraction spots are indicated. The radial sharp lines as well as the diffuse intensity along the Laue circles arise from a manifold of Kikuchi lines. The sharp spots are evident for the highly ordered surface. (b) and (c) depict line profiles along the horizontal and vertical directions as indicated in (a) as red dotted and blue solid lines, respectively. The individual diffraction spots in (b) and (c) are identified by their surface Miller indices. The dashed lines in (b) and (c) are Gaussian multipeak fits to the line profiles and are shifted vertically for clarity. The peak widths (FWHM) of the individual peaks are given in percentage Brillouin zone (100% BZ equals 1.89 Å^{-1}). The transfer width ξ is 54 and 5 nm for the horizontal and vertical directions, respectively. The large difference in the horizontal and vertical transfer width of one order of magnitude is characteristic for RHEED. Therefore, higher resolution is achieved along the horizontal direction.

space. The transfer width can be derived from the FWHM (given in Å^{-1}) of a diffraction peak with a Gaussian spot profile through $\xi = 2\pi/\mathrm{FWHM}_{\mathrm{spot}}$.[34–36] We used the bare Si(111) surface with its inherent (7 × 7) reconstruction to determine the transfer width. Since this surface can be easily prepared with huge domains of perfect (7 × 7) reconstruction, we obtain the instrumental response function not limited by the surface morphology. The diffraction pattern of the (7 × 7) reconstructed surface is shown in Fig. 5(a). It is characterized by a large number of diffraction spots and a low background intensity. In RHEED, the diffraction spots are arranged on so-called Laue circles which are centered at the shadow edge beneath the (00)-spot, i.e., the specular reflected spot.[37] Taking line profiles along (red dotted line in the diffraction pattern) and perpendicular (blue solid line in the diffraction pattern) to the Laue circles allow to determine the transfer width along these two major directions. The resulting spot profiles and their surface diffraction indices are depicted in Figs. 5(b) and 5(c). Along the Laue circle, the width of the diffraction spot amounts to 9% of the Brillouin zone which is equal to 0.17 Å^{-1}, as shown in Fig. 5(b). Perpendicular to the Laue circles, the FWHM is only 0.65% of the Brillouin-zone which is equal to 0.012 Å^{-1}, as shown in Fig. 5(c). This value is more than one order of magnitude smaller than that along the Laue circle. The transfer width is obtained by the reciprocal of the k-space resolution and amounts to $\xi_{\parallel}$ = 5 nm (this is also the expected transfer width in transmission mode) and $\xi_{\perp}$ = 54 nm along and perpendicular to the Laue circle, respectively. This large difference in the resolving power is characteristic for RHEED: the direction along the electron beam path is the high-resolution direction. Compared to our previous setup,[23] the resolution power along the beam path is increased by almost a factor of two. We attribute this improved transfer width to the small electron emission area on the photocathode in combination with the optimized magnetic lens design. Due to the high extraction field in the cathode to anode region, the virtual source image is behind the cathode and is demagnified. Altogether the source area is magnified by a factor of 1:4.6 onto the channel plate, i.e., the maximum diameter of the emission area is $d_S \approx 70\ \mu$m [cf. Fig. 2(d)].

IV. TEMPORAL RESOLUTION

In a time-resolved experiment, not only the spatial resolution but even more the temporal resolution is of crucial importance. An upper limit for the temporal resolution of our RHEED experiment has been determined from the transient changes in the spot intensity during the structural response of an optically driven phase transition. We use a prototypical atomic wire system formed by self-assembly of one atomic layer of indium atoms on a Si(111) surface.[38–42] This surface system exhibits a metal-to-insulator transition of first order at 130 K.[43–45] Below 130 K, the system is in its charge density wave (CDW) ground state with a (8 × 2) symmetry of the surface unit cell. The CDW ground state can be lifted by photoexcitation through 80 fs laser pulses of 800 nm wavelength at an incident fluence of $\Phi > 2$ mJ/cm^2 and forms a metastable metallic state that is (4 × 1) reconstructed.[30] Figure 6(a) shows the temporal evolution of the (00)-spot which is characteristic for this transformation.[32] The fit function

$$I(t) = \int_{-\infty}^{\infty} g(t-\tau) f(\tau)\, \mathrm{d}\tau, \tag{1}$$

is taken as a convolution of the atomic wire temporal response function $f(t)$ and a Gaussian $g(t)$ to account for the temporal instrumental response function (TIRF). The excitation of the CDW ground state is found to follow a mono-exponential behavior with decay time constant τ_{dec} for positive delays ($t > 0$) for all incident fluences $\Phi > 2$ mJ/cm^2. The TIRF is comparable to the cross-correlation function in an all-optical pump-probe experiment, except that here the probe pulse is an electron pulse. By describing the TIRF with a Gaussian, it is implicitly assumed that pump and probe pulses are described by Gaussians, too. The FWHM of the TIRF δ_{TIRF} is then given by

$$\delta_{\mathrm{TIRF}} = \sqrt{\delta_{\mathrm{EPW}}^2 + \delta_{\mathrm{PPW}}^2}, \tag{2}$$

with δ_{EPW} being the electron pulse width and δ_{PPW} being the pump pulse widthj the sample. Under the above made assumptions for the functions $f(t)$ and $g(t)$, an analytical expression for the intensity

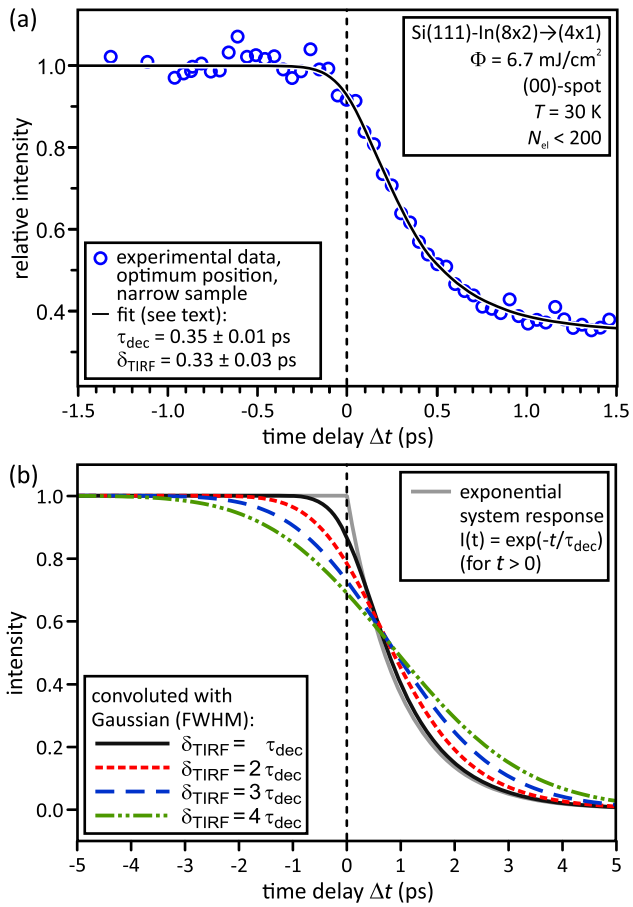

FIG. 6. Temporal evolution of the diffraction spot intensity. (a) depicts the temporal response of the relative (00)-spot intensity (open circles). An (8 × 2)-reconstructed Si(111) surface covered with 1 monolayer of indium is excited by 80 fs short laser pulses at 800 nm wavelength. An exponential decay with time constant τ_{dec} = (0.35 ± 0.01) ps convolved with a Gaussian with FWHM of δ_{TIRF} = (0.33 ± 0.03) ps fits the data (errors are given as ±1 standard deviation). (b) Response function convolved with Gaussians of different δ_{TIRF}. This Gaussian is used to describe the temporal instrumental resolution function (TIRF). The TIRF itself is the convolution of the electron probe pulse and laser pump pulse functions. For increasing δ_{TIRF}, the observed response asymptotically reaches a sigmoidal function and the exponential is smeared out.

evolution $I(t)$ can be found. This function nicely describes the data as evident by the solid line in Fig. 6(a).

The effect of the convolution with the TIRF on the intensity $I(t)$ is depicted in Fig. 6(b). First, around zero time delay ($\Delta t = 0$), the sharp edge of the system response is smeared out. Second, the observed decay constant of the exponential system response τ_{dec} increases with increasing FWHM δ_{TIRF} of the TIRF. For $\delta_{TIRF} > 3\ \tau_{dec}$, the temporal intensity evolution $I(t)$ already resembles a sigmoidal function. In this case, a reliable extraction of the system excitation time constant τ_{dec} is not possible as the temporal resolution obscures the response.

To determine the electron pulse width at the sample, an important parameter besides the dimensions of the gun and the electron energy is the electron density in the pulse. Varying the fluence of the UV laser pulse on the photocathode allows changing the number of emitted electrons N_{el} while keeping the pulses' initial volume V_{el} constant. The pulse is described as a disk of diameter $d_S \approx 70\ \mu$m (see above) and length $l_S \approx 20\ \mu$m (from the laser pulse duration), resulting in $V_{el} \approx 7.7 \times 10^{-8}$ cm^3. In Fig. 7(a), the temporal evolutions of the (00)-spot for different electron numbers N_{el} per pulse are shown. For the determination of N_{el}, a calibration of the MCP detector has been performed. Through the counting of single electrons in the MCP, a functional relationship between the MCP voltage and measured signal for a single electron detection was obtained. With this calibration, the number of electrons per pulse could be estimated, however with a large uncertainty of ±40%. In Fig. 7(a), N_{el} has been varied from approximately 550 to 38 000 electrons per

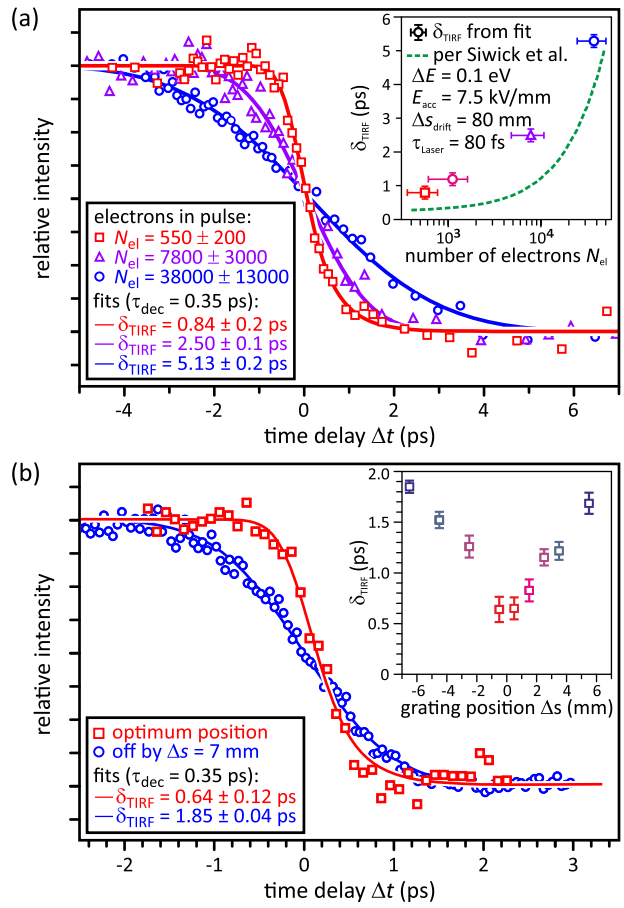

FIG. 7. (a) shows the relative intensity of the (00)-spot for 3 different numbers of electrons N_{el} in the probe pulse. For a large N_{el}, the temporal response is smeared out. For the fits of δ_{TIRF}, the decay constant τ_{dec} of the system response has been set to 0.35 ps which is the value found for the applied laser fluence.[32] The inset compares δ_{TIRF} with a model (dashed green line) by Siwick *et al.*[46] (b) The dependence of δ_{TIRF} on the lateral position of the tilt stage is shown. The optimum position is defined as the position of the stage with the smallest δ_{TIRF}. Shifting the tilt stage by 7 mm out of the optimum position, the observed system response is significantly smeared out. The inset shows δ_{TIRF} for different positions of the grating with Δs = 0 mm as the optimum position.

TABLE I. Parameters for the model calculations for the electron pulse width at the sample (cf. Siwick *et al.*).

Initial energy spread ΔE (eV)	Electric field E_{acc} (kV/mm)	Electron energy E_0 (keV)	Drift length l (cm)
0.1	7.5	30	9.4

pulse. For pulses with a high electron number N_{el}, the TIRF becomes sigmoidal. Reducing N_{el} leads to an asymmetric temporal behavior around delay zero. By fitting the above function to the data, the FWHM of the TIRF δ_{TIRF} is extracted and displayed in the inset of Fig. 7(a) with a logarithmic scale of N_{el}. The dashed line in this inset shows an analytic model for electron packet propagation developed by Siwick *et al.*[46] To evaluate the pulse duration within this model, the parameters listed in Table I have been used.

The overall trend of decreasing temporal pulse width with reduced number of electrons per pulse is explained by the model calculation: space charge repulsion causes temporal and spatial broadening of the pulse. This effect is reduced with decreasing N_{el} and ultimately has to vanish in single electron experiments.[47–50]

The experimental overall temporal resolution δ_{TIRF} is systematically larger than the model calculations. This effect is attributed to the convolution of the laser pump and electron probe pulse at the sample. To ensure surface sensitivity, electron scattering occurs at a glancing angle of incidence of $\theta = 1°–6°$. Electrons with $E_0 = 30$ keV —already traveling at 1/3 of speed of light—still need 20 ps to traverse a sample of a typical width of 2 mm. Within this time, the transient intensity changes in the RHEED pattern are averaged. This effect is known as velocity mismatch and is detrimental for achieving a high temporal resolution.[51,52] Tilting the pump pulse intensity front with respect to its propagation direction, a constant time delay between pump and probe pulses can be achieved.[14,53] Then, the resulting width of the overall temporal response function is ultimately given by the electron and laser pulse widths. The pump pulse front tilting is achieved by first order back diffraction off a blazed grating in (almost) Littrow geometry. Using a 1:1 telescope, the grating is imaged onto the sample. As a result, we obtain a tilted pump pulse front at the sample with the desired tilt angle of 71°.[54] This setup has the inherent property that the planes of constant pulse width are tilted with respect to the sample surface. Therefore, only at one vertical line on the sample, the tilted pulse is shortest due to the group delay dispersion of the laser pump pulse. Thus, only a narrow part on the sample is excited by a pump pulse with the shortest pulse width (here 80 fs). Assuming that this line is centered on the sample, the laser pulse width at the edges of a 2 mm wide sample amounts to 100 fs. Figure 7(b) reveals the extreme sensitivity of the temporal resolution on the correct geometric settings of the tilted pulse front scheme. Here, the distance between the grating and sample has been varied by several millimeters. For small deviations, the observed increase in the TIRF follows a parabolic behavior from the optimum position as expected from the group delay dispersion [see the inset of Fig. 7(b)].

To increase the temporal resolution further, we virtually reduced the probed width of the sample and decreased the number of electrons to $N_{el} < 200$/pulse. The probed width has been reduced by lateral shifts of the sample out of the interaction region to the point where the (00)-spot is barely visible. The best result achieved is shown in Fig. 6(a) with a data acquisition time of 2 h for 80 data points. The resulting optimum TIRF is 330 ± 30 fs (FWHM) which is slightly larger than the theoretically achievable temporal resolution of 275 fs. This value is obtained from the asymptotic behavior of the electron pulse width of 264 fs for $N_{el} \to 1$ and a temporal width of the tilted pulse front which is equal to those of the initial laser pulse width of 80 fs using Eq. (2).

V. SUMMARY

We presented the properties of our third generation pulsed electron gun which was designed to be a reliable source for time-resolved electron diffraction experiments at surfaces. The electron gun operates at 30 kV without any electron pulse compression scheme. The transverse coherence length of the gun is 54 nm in the high resolution direction and 5 nm in the perpendicular direction. The high coherence length is achieved through focusing the UV pulse onto the photocathode leading to a small source size of the electrons. The overall temporal resolution is determined by the cross correlation between the light pump and electron probe pulses. The highest temporal resolution has been achieved for less than 200 electrons per pulse and a narrow sample width. For these settings, the overall temporal resolution of the entire experimental setup is 330 fs (FWHM) which is only slightly larger than the theoretically achievable temporal resolution of 275 fs. At increased electron number per pulse $N_{el} = 1000$, the pulse duration is still in the sub-picosecond regime. The wide range of operating conditions from a maximum achievable temporal resolution at small electron numbers to high intensity at reduced temporal resolution makes this gun an ideal pulsed electron source for daily use. In addition, we found that the In/Si(111) surface system is ideally suited to serve as a pump-probe correlator for electron diffraction at surfaces to benchmark the performance of the experimental setup.

ACKNOWLEDGMENTS

Fruitful discussion with G. Sciaini, B. Krenzer, and T. Frigge and technical support from H. Wolf, L. Kujawinski, and the university workshop as well as gratuitous support from Vacuumschmelze GmbH & Co. KG through the annealing of the lens assembly is greatly appreciated. Financial support via funding from the Deutsche Forschungsgemeinschaft (DFG, German Research Foundation)—Projekt No. 5485074—SFB 616 with sub-project B02 "Dynamics of Surface Atoms after Electronic excitation" and DFG—Projekt No. 278162697—SFB1242 sub-project C03 "Driven phase transitions at surfaces: initial dynamics, hidden states and relaxation" is gratefully acknowledged.

REFERENCES

[1] P. S. Kirchmann, L. Rettig, X. Zubizarreta, V. M. Silkin, E. V. Chulkov, and U. Bovensiepen, Nat. Phys. **6**, 782 (2010).
[2] C. W. Nicholson, A. Lücke, W. G. Schmidt, M. Puppin, L. Rettig, R. Ernstorfer, and M. Wolf, Science **362**, 821 (2018).
[3] C. W. Siders, A. Cavalleri, K. Sokolowski-Tinten, C. Tóth, T. Guo, M. Kammler, M. Horn-von Hoegen, K. R. Wilson, D. v. d. Linde, and C. P. J. Barty, Science **286**, 1340 (1999).

[4]K. Sokolowski-Tinten, C. Blome, J. Blums, A. Cavalleri, C. Dietrich, A. Tarasevitch, I. Uschmann, E. Förster, M. Kammler, M. Horn-von Hoegen, and D. von der Linde, Nature **422**, 287 (2003).
[5]J. M. Thomas, Angew. Chem., Int. Ed. **43**, 2606 (2004).
[6]J. R. Dwyer, C. T. Hebeisen, R. Ernstorfer, M. Harb, V. B. Deyirmenjian, R. E. Jordan, and R. Dwayne Miller, Philos. Trans. R. Soc., A **364**, 741 (2006).
[7]R. J. D. Miller, Science **343**, 1108 (2014).
[8]H. Ihee, V. A. Lobastov, U. M. Gomez, B. M. Goodson, R. Srinivasan, C.-Y. Ruan, and A. H. Zewail, Science **291**, 458 (2001).
[9]R. Srinivasan, J. S. Feenstra, S. T. Park, S. Xu, and A. H. Zewail, Science **307**, 558 (2005).
[10]M. Gao, C. Lu, H. Jean-Ruel, L. C. Liu, A. Marx, K. Onda, S.-y. Koshihara, Y. Nakano, X. Shao, T. Hiramatsu, G. Saito, H. Yamochi, R. R. Cooney, G. Moriena, G. Sciaini, and R. J. D. Miller, Nature **496**, 343 (2013).
[11]B. J. Siwick, J. R. Dwyer, R. E. Jordan, and R. J. D. Miller, Science **302**, 1382 (2003).
[12]R. Ernstorfer, M. Harb, C. T. Hebeisen, G. Sciaini, T. Dartigalongue, and R. J. D. Miller, Science **323**, 1033 (2009).
[13]G. Sciaini, M. Harb, S. G. Kruglik, T. Payer, C. T. Hebeisen, F.-J. M. z. Heringdorf, M. Yamaguchi, M. Horn-von Hoegen, R. Ernstorfer, and R. J. D. Miller, Nature **458**, 56 (2009).
[14]P. Baum, D.-S. Yang, and A. H. Zewail, Science **318**, 788 (2007).
[15]M. Eichberger, H. Schäfer, M. Krumova, M. Beyer, J. Demsar, H. Berger, G. Moriena, G. Sciaini, and R. J. D. Miller, Nature **468**, 799 (2010).
[16]V. R. Morrison, R. P. Chatelain, K. L. Tiwari, A. Hendaoui, A. Bruhács, M. Chaker, and B. J. Siwick, Science **346**, 445 (2014).
[17]R. P. Chatelain, V. R. Morrison, B. L. M. Klarenaar, and B. J. Siwick, Phys. Rev. Lett. **113**, 235502 (2014).
[18]M. J. Stern, L. P. René de Cotret, M. R. Otto, R. P. Chatelain, J.-P. Boisvert, M. Sutton, and B. J. Siwick, Phys. Rev. B **97**, 165416 (2018).
[19]S. Vogelgesang, G. Storeck, J. G. Horstmann, T. Diekmann, M. Sivis, S. Schramm, K. Rossnagel, S. Schäfer, and C. Ropers, Nat. Phys. **14**, 184 (2017).
[20]C.-Y. Ruan, F. Vigliotti, V. A. Lobastov, S. Chen, and A. H. Zewail, Proc. Natl. Acad. Sci. U. S. A. **101**, 1123 (2004).
[21]V. Franco, C. Songye, R. Chong-Yu, V. A. Lobastov, and A. H. Zewail, Angew. Chem., Int. Ed. **43**, 2705 (2004).
[22]C.-Y. Ruan, V. A. Lobastov, F. Vigliotti, S. Chen, and A. H. Zewail, Science **304**, 80 (2004).
[23]A. Janzen, B. Krenzer, O. Heinz, P. Zhou, D. Thien, A. Hanisch, F.-J. Meyer zu Heringdorf, D. von der Linde, and M. Horn-von Hoegen, Rev. Sci. Instrum. **78**, 013906 (2007).
[24]A. Hanisch-Blicharski, A. Janzen, B. Krenzer, S. Wall, F. Klasing, A. Kalus, T. Frigge, M. Kammler, and M. Horn-von Hoegen, Ultramicroscopy **127**, 2 (2013), frontiers of Electron Microscopy in Materials Science.
[25]W. Liang, S. Schäfer, and A. H. Zewail, Chem. Phys. Lett. **542**, 1 (2012).
[26]B. Krenzer, A. Janzen, P. Zhou, D. von der Linde, and M. Horn-von Hoegen, New J. Phys. **8**, 190 (2006).
[27]T. Frigge, B. Hafke, V. Tinnemann, T. Witte, and M. Horn-von Hoegen, Struct. Dyn. **2**, 035101 (2015).
[28]T. Witte, T. Frigge, B. Hafke, B. Krenzer, and M. Horn-von Hoegen, Appl. Phys. Lett. **110**, 243103 (2017).
[29]S. Sakong, P. Kratzer, S. Wall, A. Kalus, and M. Horn-von Hoegen, Phys. Rev. B **88**, 115419 (2013).
[30]S. Wall, B. Krenzer, S. Wippermann, S. Sanna, F. Klasing, A. Hanisch-Blicharski, M. Kammler, W. G. Schmidt, and M. Horn-von Hoegen, Phys. Rev. Lett. **109**, 186101 (2012).
[31]T. Frigge, B. Hafke, T. Witte, B. Krenzer, and M. Horn-von Hoegen, Struct. Dyn. **5**, 025101 (2018).
[32]T. Frigge, B. Hafke, T. Witte, B. Krenzer, C. Streubühr, A. Samad Syed, V. Miksic Trontl, I. Avigo, P. Zhou, M. Ligges, D. von der Linde, U. Bovensiepen, M. Horn-von Hoegen, S. Wippermann, A. Lücke, S. Sanna, U. Gerstmann, and W. G. Schmidt, Nature **544**, 207 (2017).
[33]R. Trebino, *Frequency-Resolved Optical Gating: The Measurement of Ultrashort Laser Pulses* (Springer, 2002).
[34]G. Comsa, Surf. Sci. **81**, 57 (1979).
[35]G.-C. Wang and M. Lagally, Surf. Sci. **81**, 69 (1979).
[36]R. L. Park, J. E. Houston, and D. G. Schreiner, Rev. Sci. Instrum. **42**, 60 (1971).
[37]W. Braun, *Applied RHEED: Reflection High Energy Electron Diffraction During Crystal Growth* (Springer, 2013).
[38]H. W. Yeom, S. Takeda, E. Rotenberg, I. Matsuda, K. Horikoshi, J. Schaefer, C. M. Lee, S. D. Kevan, T. Ohta, T. Nagao, and S. Hasegawa, Phys. Rev. Lett. **82**, 4898 (1999).
[39]O. Bunk, G. Falkenberg, J. H. Zeysing, L. Lottermoser, R. L. Johnson, M. Nielsen, F. Berg-Rasmussen, J. Baker, and R. Feidenhans'l, Phys. Rev. B **59**, 12228 (1999).
[40]C. Kumpf, O. Bunk, J. H. Zeysing, Y. Su, M. Nielsen, R. L. Johnson, R. Feidenhans'l, and K. Bechgaard, Phys. Rev. Lett. **85**, 4916 (2000).
[41]S. V. Ryjkov, T. Nagao, V. G. Lifshits, and S. Hasegawa, Surf. Sci. **488**, 15 (2001).
[42]W. G. Schmidt, S. Wippermann, S. Sanna, M. Babilon, N. J. Vollmers, and U. Gerstmann, Phys. Status Solidi B **249**, 343 (2011).
[43]S. J. Park, H. W. Yeom, S. H. Min, D. H. Park, and I. W. Lyo, Phys. Rev. Lett. **93**, 106402 (2004).
[44]F. Klasing, T. Frigge, B. Hafke, B. Krenzer, S. Wall, A. Hanisch-Blicharski, and M. Horn-von Hoegen, Phys. Rev. B **89**, 121107 (2014).
[45]J. Yeo, H. Shim, and G. Lee, J. Vac. Sci. Technol., A **31**, 061402 (2013).
[46]B. J. Siwick, J. R. Dwyer, R. E. Jordan, and R. J. D. Miller, J. Appl. Phys. **92**, 1643 (2002).
[47]L. Kasmi, D. Kreier, M. Bradler, E. Riedle, and P. Baum, New J. Phys. **17**, 033008 (2015).
[48]S. Lahme, C. Kealhofer, F. Krausz, and P. Baum, Struct. Dyn. **1**, 034303 (2014).
[49]Y. Morimoto and P. Baum, Nat. Phys. **14**, 252 (2018).
[50]C. Kealhofer, W. Schneider, D. Ehberger, A. Ryabov, F. Krausz, and P. Baum, Science **352**, 429 (2016).
[51]J. C. Williamson and A. H. Zewail, Chem. Phys. Lett. **209**, 10 (1993).
[52]P. Zhang, J. Yang, and M. Centurion, New J. Phys. **16**, 083008 (2014).
[53]P. Baum and A. H. Zewail, Proc. Natl. Acad. Sci. U. S. A. **103**, 16105 (2006).
[54]P. Zhou, C. Streubühr, A. Kalus, T. Frigge, S. Wall, A. Hanisch-Blicharski, M. Kammler, M. Ligges, U. Bovensiepen, D. von der Linde, and M. Horn-von Hoegen, EPJ Web Conf. **41**, 10016 (2013).